The Astrophysical Journal, 725:1327–1336, 2010 December 10 doi:10.1088/0004-637X/725/1/1327

STAR FORMATION IN THE TAURUS FILAMENT L 1495: FROM DENSE CORES TO STARS*

Markus Schmalzl[1], Jouni Kainulainen[1], Sascha P. Quanz[2], João Alves[3], Alyssa A. Goodman[4], Thomas Henning[1], Ralf Launhardt[1], Jaime E. Pineda[4], and Carlos G. Román-Zúñiga[5]
[1] Max-Planck-Institut für Astronomie, Königstuhl 17, 69117 Heidelberg, Germany; schmalzl@mpia.de
[2] Institute for Astronomy-Swiss Federal Institute of Technology (ETH), Wolfgang-Pauli-Strasse 27, 8093 Zurich, Switzerland
[3] University of Vienna, Türkenschanzstrasse 17, 1180 Vienna, Austria
[4] Harvard-Smithsonian Center for Astrophysics, 60 Garden Street, MS 42, Cambridge, MA 02138, USA
[5] Centro Astronómico Hispano Alemán/Instituto de Astrofísica de Andalucía (IAA-CSIC), Glorieta de la Astronomía, S/N, Granada 18008, Spain
Received 2010 July 6; accepted 2010 October 11; published 2010 November 24

ABSTRACT

We present a study of dense structures in the L 1495 filament in the Taurus Molecular Cloud and examine its star-forming properties. In particular, we construct a dust extinction map of the filament using deep near-infrared observations, exposing its small-scale structure in unprecedented detail. The filament shows highly fragmented substructures and a high mass-per-length value of $M_{\rm line} = 17\,M_{\odot}\,{\rm pc}^{-1}$, reflecting star-forming potential in all parts of it. However, a part of the filament, namely B 211, is remarkably devoid of young stellar objects. We argue that in this region the initial filament collapse and fragmentation is still taking place and star formation is yet to occur. In the star-forming part of the filament, we identify 39 cores with masses from 0.4 to 10 $M_{\odot}$ and preferred separations in agreement with the local Jeans length. Most of these cores exceed the Bonnor–Ebert critical mass, and are therefore likely to collapse and form stars. The dense core mass function follows a power law with exponent $\Gamma = 1.2 \pm 0.2$, a form commonly observed in star-forming regions.

Key words: dust, extinction – ISM: clouds – ISM: individual objects (L1495) – ISM: structure – stars: formation

1. INTRODUCTION

Filaments appear to be common structural features in both quiescent and star-forming molecular clouds. In particular, recent observations of molecular clouds with *Herschel* (Pilbratt et al. 2010) have signified the role of filaments as a momentous, perhaps even dominant mode of star formation (e.g., Henning et al. 2010; Molinari et al. 2010; Men'shchikov et al. 2010). However, their formation and small-scale structure are still not well understood and under debate (see, e.g., Myers 2009, and references therein). Schneider & Elmegreen (1979) noted that filaments tend to fragment into equally spaced condensations of sizes $\sim 10^{0}$ pc. These clumps, in turn, consist of even smaller, gravitationally bound entities, namely cores, of size $\sim 10^{-1}$ pc, which are of the order of the local Jeans length. These cores are then believed to be the direct precursors of stars and binary systems (see review by Bergin & Tafalla 2007).

Such a hierarchical structure can also be found in the Taurus Molecular Cloud (Figure 1), which is one of the closest star-forming regions at a distance of only 137 ± 10 pc (Torres et al. 2007), and therefore an excellent test bed to study the small-scale structure of filaments. Large-scale surveys in CO (Mizuno et al. 1995; Onishi et al. 1998; Narayanan et al. 2008) and mid-infrared dust emission (Rebull et al. 2010), alongside of dust extinction maps (Dobashi et al. 2005; Kainulainen et al. 2009a; Lombardi et al. 2010) have built a detailed view of a complex network of filaments in Taurus, which are known to be the birth sites of stars (see reviews about star formation in Taurus by, e.g., Palla & Stahler 2002; Kenyon et al. 2008). These filaments are composed of clumps (Barnard 1927; Lynds 1962; Lee & Myers 1999) with sizes of $\sim$1 pc, which host a plethora of cores with typical sizes of $\sim$0.1 pc. These have been detected, e.g., via molecular line observations tracing cold and dense gas with volume densities of $n_{\rm H_2} \gtrsim 10^{5}\,{\rm cm}^{-3}$, such as NH_3 (Jijina et al. 1999) and $H^{13}CO^{+}$ (Onishi et al. 2002, hereafter OMK02). Further down in this hierarchical structure, from dust continuum observations Sadavoy et al. (2010) found a population of pre- and protostellar cores, supposedly representing the scale of direct core–protostar connection. The Taurus Molecular Cloud is known to host $\gtrsim$250 young stellar objects (YSOs; Rebull et al. 2010), and their distribution shows a strong correlation to the filamentary structures, i.e., their birth sites (Hartmann 2002; Kenyon et al. 2008).

To further understand the connection between filamentary structures and star formation, it is essential to characterize the filament in high spatial resolution over a wide dynamic range. Molecular line species can be used as probes for column densities, but typically rather exhibit a narrow dynamical range. A larger dynamical range can be achieved by thermal dust emission observations, which are used to trace intermediate to high column densities, and dust extinction mapping, which is more sensitive at low to intermediate column density range (see, e.g., Pineda et al. 2008; Goodman et al. 2009; Vasyunina et al. 2009, for a comparison of different methods). The aforementioned observations allow us to determine the structure of the low-density clumps on one hand, and the core population detected by dense gas tracers on the other hand. However, to make a direct connection between the diffuse envelope structure and the denser cores, one preferably needs a single tracer with a uniform calibration, which covers both these regimes.

Therefore, the aim of this work is to create a column density map of L 1495 (Lynds 1962) with unprecedented dynamical range and resolution with the aid of near-infrared (NIR) dust extinction mapping. NIR colors of stars in the background of clouds provide hundreds to thousands of pencil-beam measurements of reddening, which can be smoothed out to construct maps of column density along a molecular cloud. This is the basis of the NIR excess technique NICE and its derivatives (Lada et al. 1994; Lombardi & Alves 2001; Foster et al. 2008;

* Based on observations collected at the German–Spanish Astronomical Center, Calar Alto, jointly operated by the Max-Planck-Institut für Astronomie Heidelberg and the Instituto de Astrofísica de Andalucía (CSIC).

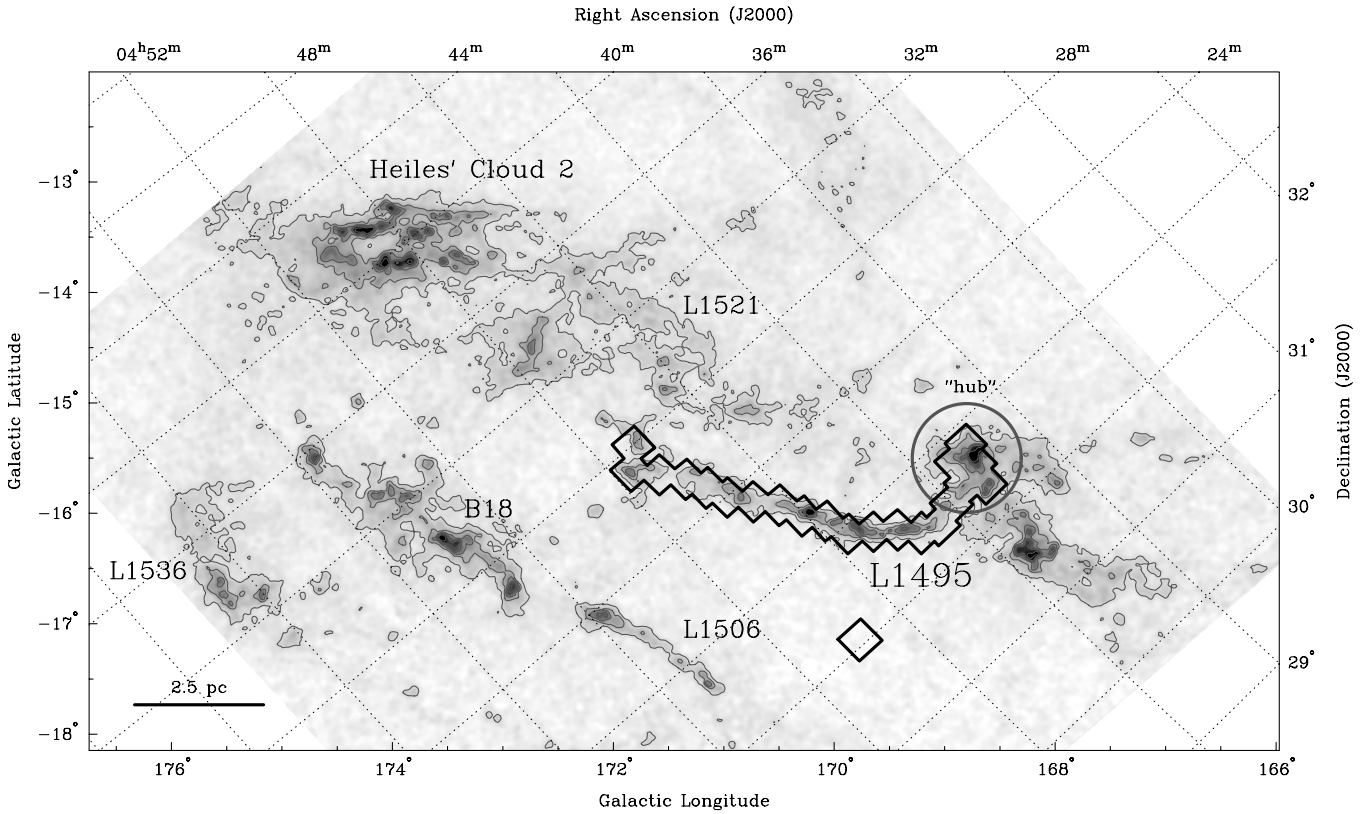

Figure 1. Extinction map of the Taurus Molecular Cloud (Kainulainen et al. 2009a) derived from 2MASS data. Contours are plotted in steps of $A_V = 2$ mag. The circle marks the center of the *hub-filament* system in L 1495 (Myers 2009) with three filaments emanating toward the east, southwest, and west. The thick solid lines mark the region of our Omega2000 observations in L 1495, and the control field to the south of it.

Lombardi 2009), which obtain extinction measurements by correlating the observations from the science field with a nearby control field. The color excess with respect to this control field is then completely attributed to be caused by the molecular cloud. These methods typically probe extinctions $A_V \sim 0.5$–50 mag (e.g., Lombardi & Alves 2001; Kainulainen et al. 2006, 2007; Román-Zúñiga et al. 2009), allowing us to examine both the detailed fragmentation of the filament into dense cores, and the envelopes surrounding them. Thus, the observations presented in this paper will provide the most complete census of the small-scale structures in the Taurus filament so far, and shed more light on the link between filaments and star-forming cores.

The paper is organized as follows. In Section 2, we give an overview of the observations and data reduction. In Section 3, we present our NIR extinction map of unprecedented depth and resolution, and derive the dense core population, which is discussed in section Section 4. Finally, the conclusions and summary follow in Section 5.

2. OBSERVATIONS AND DATA REDUCTION

We carried out NIR observations of the Taurus filament L 1495 with the Omega2000 camera at the Calar Alto 3.5 m telescope. The camera is equipped with a HAWAII2 HgCdTe detector that offers 2048 × 2048 pixels with a pixel scale of 0.″45 and a field of view of 15.′4 × 15.′4. Observations were carried out during two observing periods from 2004 October to 2005 December (Quanz et al. 2010) and 2009 January to March. In total, 21 science fields and 1 control field were observed in the J, H, and K_s bands (1.2 μm, 1.6 μm, and 2.2 μm, respectively). The locations of the observed frames are shown in Figure 1.

The observations of a single Omega2000 field consisted of 30 dithered exposures, each having an integration time of 60 s. This resulted in total exposure times of 30 minutes per filter per field. We performed a standard NIR data reduction with the Omega2000 pipeline (Fassbender 2003), including flat-field, dark and bad pixel corrections, sky subtraction, and image registering. The world coordinate system (WCS) was appended to the frames with `koords` (Gooch 1996) by matching the positions of at least 10 stars per frame to matching stars from the corresponding Two Micron All Sky Survey (2MASS) image. This resulted to the rms accuracy of 0.1 pixels (or 0.″045) in all frames.

In addition to stars, a significant amount of background galaxies was expected to be detected in the frames. In order to disentangle these two types of sources, we performed photometry using SExtractor (Bertin & Arnouts 1996), which provides an automatic source classification via the so-called *stellarity index* (`CLASS_STAR`). In particular, photometry was run in a fully automated two-pass mode. First, SExtractor was run for the brightest stars only, in order to get an accurate estimate of the seeing, which is a crucial input parameter to get reliable measures of the stellarity index, and furthermore determined our choice of aperture size. Second, the actual photometry was performed, resulting in instrumental magnitude and uncertainty, position, the stellarity index C, elongation E (the inverse of the aspect ratio) and the parameter F_0, which is a source's FWHM normalized by the seeing.

Each source was classified as either a star or a galaxy following the classification scheme from Cantiello et al. (2005). In this scheme, a source is regarded as a *star* if it fulfills two out of the three following conditions:

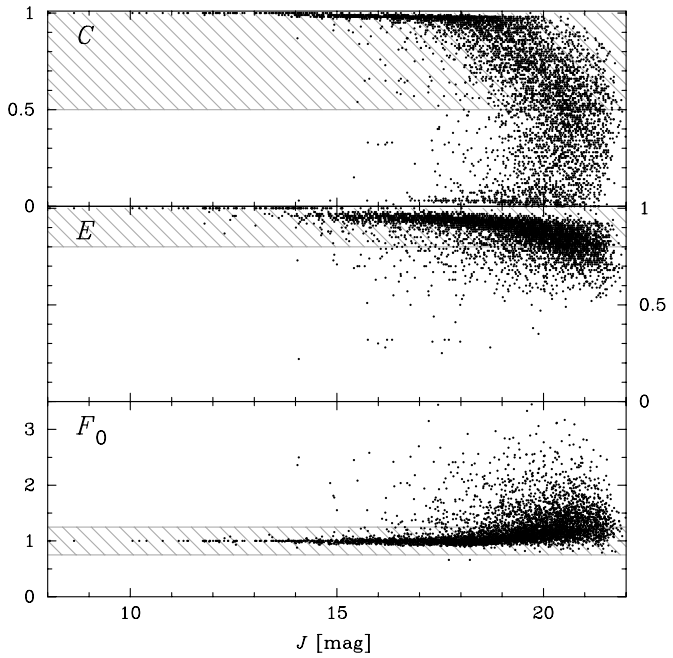

Figure 2. Our star–galaxy separation is based on the stellarity index C, elongation E, and its normalized FWHM F_0. The hatched areas indicate the regions populated by stars. Due to illustrative reasons, only a small part of our final catalog is shown.

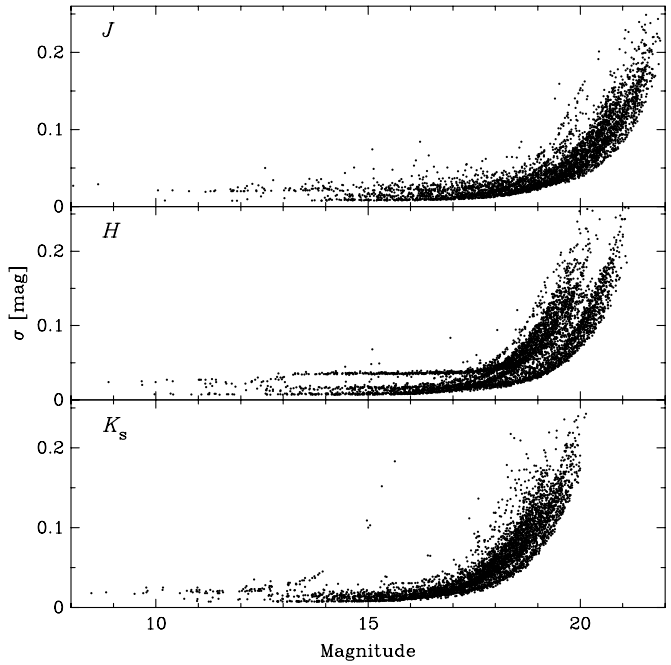

Figure 3. Photometric uncertainties for our sources in different filters. They contain contributions from the photometric error and the uncertainty of their individual photometric zero point. This figure clearly shows the contributions from different frames, which differ in terms of sensitivity due to varying observing conditions. Due to illustrative reasons, only a small part of our final catalog is shown.

1. $C > 0.5$
2. $E > 0.8$
3. $0.75 < F_0 < 1.25$

which are indicated as hatched regions in Figure 2.

The photometric calibration was done for each frame separately by matching sources within the frame with stars from the 2MASS catalog, and determining photometric zero points and color corrections using those stars. These catalogs in J, H, and K_s were then merged, and sources with a detection in only one filter were rejected. Saturated stars were replaced by their 2MASS counterparts. The final catalog of L 1495 contains ~33,000 sources, of which 63% are classified as stars, according to our classification scheme. Photometric uncertainties for an excerpt from this catalog are shown in Figure 3. The median magnitudes for which $\sigma = 0.1$ mag are at $J = 20.6$ mag, $H = 19.4$ mag, and $K_s = 18.8$ mag, which is on average 4 mag deeper than 2MASS, and emphasizes the depth of our observations.

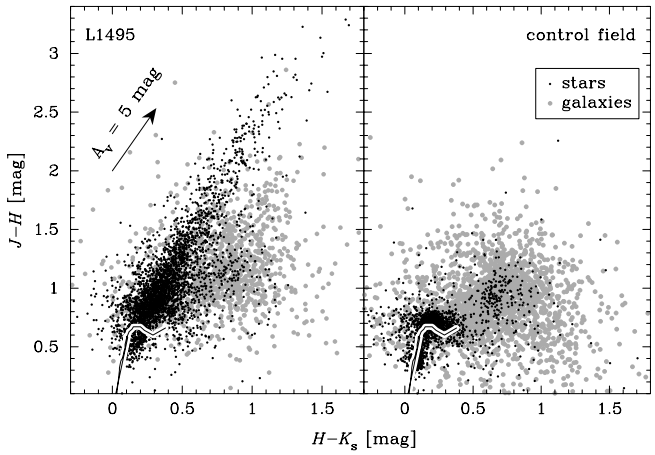

Figure 4. NIR color–color diagram of the science (left) and the control field (right). A shift caused by an extinction of $A_V = 5$ mag (assuming the reddening law of Rieke & Lebofsky 1985) is indicated by the arrow in the left panel. The continuous line shows an unreddened ZAMS (Siess et al. 2000) for comparison.

3. RESULTS

3.1. Dust Extinction in the Taurus Filament

We used the JHK_s photometry of the detected sources to derive dust extinction through the Taurus filament L 1495. In the following, we first shortly describe the adopted technique and then present the results.

As mentioned earlier, in addition to stars there is a significant number of background galaxies among detected sources. The intrinsic colors of galaxies are very different from those of stars, and therefore theses two classes need to be treated separately in deriving extinction toward them. This difference is illustrated in Figure 4, which shows color–color diagrams of our reference (right panel) and one science field (left panel). Especially in the reference field, one can clearly see the different color distribution of stars and galaxies, as it is unaffected by the dust extinction from the molecular cloud. We note that there is a concentration of stars at $[H - K_s, J - H] = [0.7, 1.0]$ that is clearly outside the zero-age main sequence (ZAMS) of stars. These sources could be YSOs, brown dwarfs, or even point-like distant galaxies and or quasars.

Recently, Foster et al. (2008) presented an NIR color-excess mapping technique tailored specifically for inclusion of galaxies. In this technique, the *colors of stars* behind the cloud are compared to the intrinsic colors of stars in the reference field. In addition, the *magnitude-dependent colors* of *galaxies* are compared to those in the reference field. This comparison yields a pencil-beam-like extinction value toward each source (for further details we refer to Foster et al. 2008). From these values we then generate a uniformly gridded extinction map by smoothing the data using a Gaussian kernel. Sigma-clipping removes

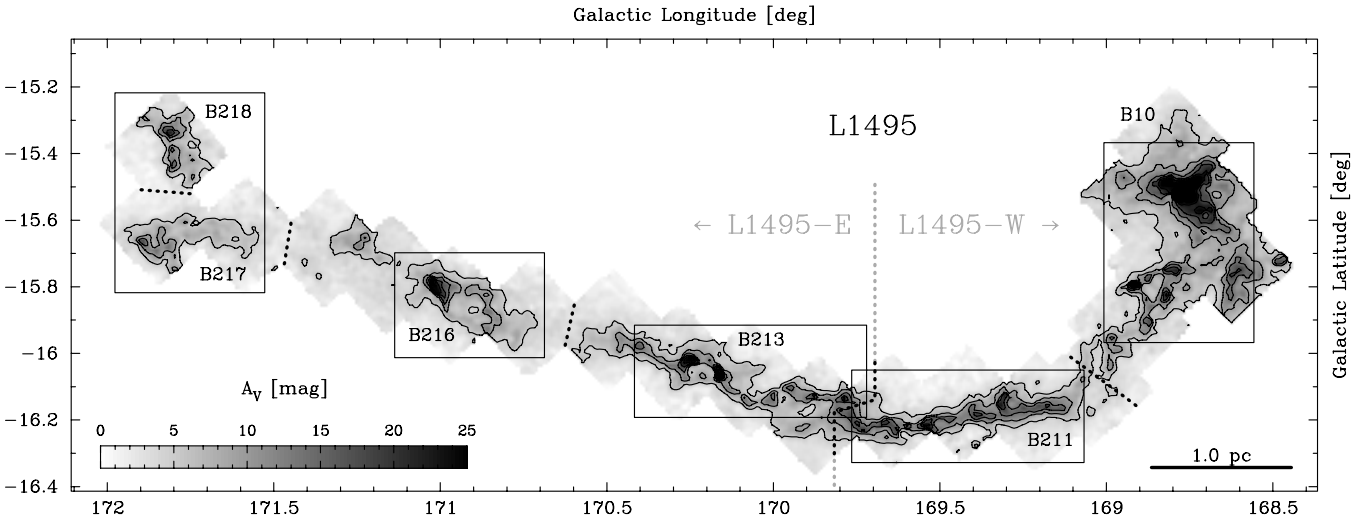

Figure 5. Extinction map of the Filament L 1495 with a resolution of 0.′9 derived from deep NIR observations with Omega2000. Contours are plotted in steps of $A_V = 5$ mag. We separate the filament into different subregions, which conform to Barnard's dark objects (Barnard et al. 1927). The boxes indicate the positions of the zoom-ins shown in Figure 6.

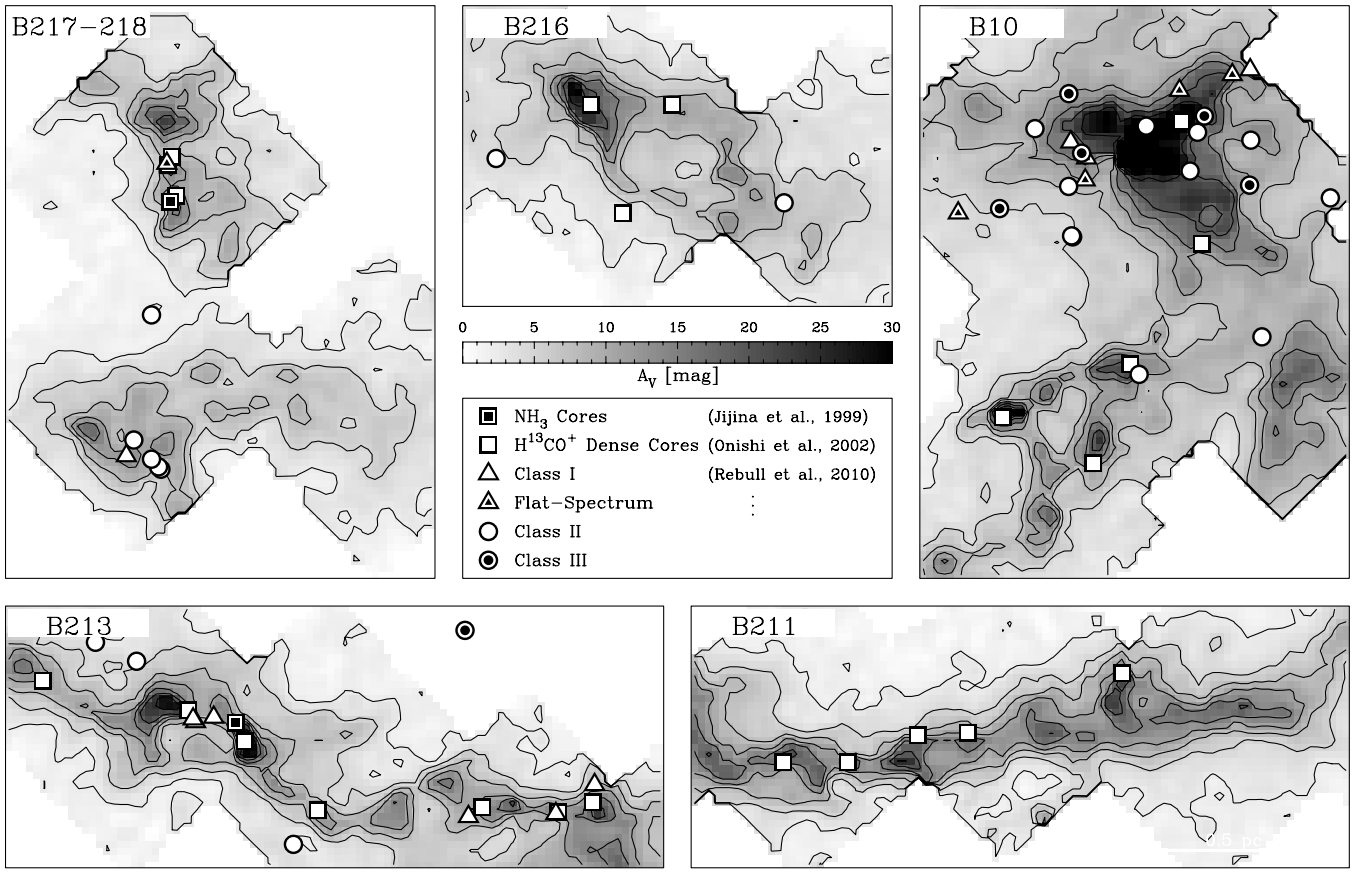

Figure 6. Zoom-ins into the extinction map. The scale bar indicated in the bottom panel is common to all sub-plots. Contours are plotted in steps of 5σ each. The positions of dense cores mapped in NH_3 (Jijina et al. 1999) and $H^{13}CO^+$ (OMK02) are overplotted alongside YSOs (Rebull et al. 2010).

sources with outliers in extinction, which might be caused by intrinsically different colors (e.g., YSOs, brown dwarfs, etc.). For our map, we chose a resolution of 0.′9 as a compromise between resolving the small-scale structures in the filament and having low noise over the dynamical range covering most of the map. In this resolution, the map covered the dynamical range of $A_V = 1.5$–35 mag. The noise of the final map depends on extinction, being $\sigma = 0.5$ mag at $A_V = 0$ mag and $\sigma = 2$ mag at $A_V = 35$ mag.

Figure 5 shows the resulting extinction map, with blowups of different regions of it shown in Figure 6. The map reveals, on one hand, a remarkably well-defined, high aspect ratio filamentary structure and, on the other hand, complex clumpy substructures within this filament. We note that within the mapped region we find six Barnard objects, namely the clumps B 211, B 213, B 216, B 217, B 218 (which represent the *filament*), and B 10 (which forms the *hub*).

Table 1
Barnard Objects in the L 1495 Filament

Region	Mass ($M_\odot$)	Area (pc^2)	Σ_M[a] ($M_\odot$ pc^{-2})
B 211	84 ± 5	0.40 ± 0.06	210.7 ± 14.8
B 213	87 ± 6	0.48 ± 0.07	180.3 ± 12.6
B 216	57 ± 4	0.34 ± 0.05	169.8 ± 11.9
B 217	29 ± 2	0.19 ± 0.03	154.8 ± 10.8
B 218	22 ± 1	0.13 ± 0.02	174.8 ± 12.2
Total	280 ± 19	1.54 ± 0.22	182.3 ± 12.8

Notes. All parameters are calculated for regions with $A_V \geqslant 5$ mag.
[a] Values for mass and area in the table are rounded, and therefore their division leads to different values compared to the correct calculation.

Within the filament, the lowest completely mapped isocontour is at $A_V = 5$ mag. The total mass within this region is $280 \pm 19\,M_\odot$, yielding a mass surface density of $\Sigma_M = 182 \pm 13\,M_\odot\,\mathrm{pc}^{-2}$. In Table 1 these parameters are also listed separately for the subregions. The mass was estimated from the extinction map by assuming all hydrogen in molecular form and the standard conversion factor of $N_{H_2}/A_V = 0.94 \times 10^{21}\,\mathrm{cm}^{-2}\,\mathrm{mag}^{-1}$ (Bohlin et al. 1978; Rieke & Lebofsky 1985), which then yields the total hydrogen mass

$$\frac{M_H}{M_\odot} = 4.89 \times 10^{-3} \left(\frac{D}{137\,\mathrm{pc}}\right)^2 \left(\frac{\theta}{0\farcm45}\right)^2 \sum_i \left(\frac{A_{V,i}}{1\,\mathrm{mag}}\right), \quad (1)$$

where D is the distance to the cloud, θ is the pixel scale of the map, and $A_{V,i}$ are the extinction values of the individual pixels. Using a standard cloud composition of 63% hydrogen, 36% helium, and 1% dust (Lombardi et al. 2006), one can assume the total mass from Equation (1) to be

$$M_{tot} = 1.37\,M_H. \quad (2)$$

The blowups shown in Figure 6 reveal numerous dense fragments with peak extinction values of $A_V \gtrsim 15$ mag. This population of *dense cores*[6] will be investigated in more detail in the following section. The main filament is strongly meandering along almost its entire length of 8 pc, and sometimes forms even ring-like structures (e.g., B 216 and B 10). However, B 211 is different in that it exhibits a linear, narrow *bar* with a length of 1.5 pc and a median FWHM of only 0.11 pc. The inter-core regions also show considerably higher extinction values of $A_V \gtrsim 10$ mag in contrast to the other parts of the filament, where cores seem to be rather isolated.

3.2. The Dense Core Population

Identification and characterization of small-scale structures, such as cores, from two-dimensional data (e.g., extinction maps or continuum observations) is a long-lasting, non-trivial problem, and several methods exist (e.g., Stutzki & Guesten 1990; Williams et al. 1994) for this. We adopted a two-step approach, which consisted of background removal and two-dimensional thresholding. In the first step, we performed a subtraction of large-scale structures from the map using wavelet filtering. This resulted in a map describing structures only at spatial scales smaller than 0.14 pc ("cores-only" map, cf., Alves et al. 2007). In the second step, we used the two-dimensional thresholding algorithm CLUMPFIND2D (Williams et al. 1994) to identify a population of dense cores from the cores-only map. The algorithm works by first contouring the data (usually these levels are defined by a detection threshold, and subsequent contours with separations of multiples of the rms noise of the observations), and then searches for peaks of emission, which mark the cores. It then follows these down to lower intensities, assigning every pixel to a certain core (if any). Obviously, such an algorithm works best for isolated cores. Pineda et al. (2009) pointed out that for observations, where one has to deal with blending of cores, CLUMPFIND2D is very sensitive to the choice of input parameters. Therefore, we ran a set of calculations with different values of detection thresholds and level separations. We performed various tests, which included visual verification of the positions, sizes, and shapes of the cores. A detection threshold and a level separation of 3σ was chosen to yield a representative core distribution. This is in agreement with the simulations by Kainulainen et al. (2009b), in which such parameters resulted in an acceptable core identification.

However, the narrow *bar* in B 211 was not removed by the wavelet filter, eventually not allowing a look at the "naked cores." This prohibited a reliable recovery of the dense cores and their properties in B 211. We believe that this is caused by its different structure, which is discussed in more detail in Section 4.1. Therefore, we did not consider this region in the following investigation. Furthermore, we also did not take into account B 10 because of its cluster-like nature and very high extinction, that does not allow us to break the structure into separate cores (Kainulainen et al. 2009b). Follow-up analysis using *dendrograms* (Rosolowsky et al. 2008) on three-dimensional position–position–velocity molecular line data might allow us to also disentangle the dense core population in these two regions in the western part (L 1495–W). In this paper, however, due to the limitations of two-dimensional data we restrict our analysis to the dense core population in the eastern part (L 1495–E), which consists of regions B 213, B 216, B 217, and B 218.

In total 39 cores were detected in L 1495–E (Figure 7, Table 2). We calculated the core orientation together with the zeroth, first, and second moment, which after suitable conversions conformed to the core mass, position, and FWHM along the minor and major axes. Furthermore, we defined the effective radius as $r_{eff} = (A/\pi)^{1/2}$, assuming spherical symmetry. We note that the mass is quite insensitive for the choice of the threshold level, changing on average only 15% when going from 3σ to 6σ. A few cores (23, 29, and 35) extended beyond our mapped region. We used data from the 2MASS catalog to extend the map to cover these cores completely.

The nearest neighbor separation of the cores exhibits a strong peak at 0.13 pc with a dispersion of 0.04 pc, and all cores had at least one neighbor within 0.25 pc. Another approach to quantify the "clustering" is to measure the two-point correlation function (e.g., Johnstone et al. 2000; Hartmann 2002), where the number of core pairs N with separations in the interval $[\log(r), \log(r) + d\log(r)]$ is compared to the number N_0 in a sample, where cores were randomly distributed over the whole region. The two-point correlation function is then

$$w(r) = \frac{N}{N_0} - 1.$$

Applying this to our sample of cores, strong correlations, i.e., $w(r) > 0$, on separations of $r \sim 0.15$ pc and $r \sim 5$ pc are

[6] Our analysis (Section 4.2) shows that these are indeed dense cores, i.e., gravitationally bound entities with densities of $n_{H_2} \sim 10^4$ cm^{-3}. Therefore, we already introduce this term here, for reasons of consistency.

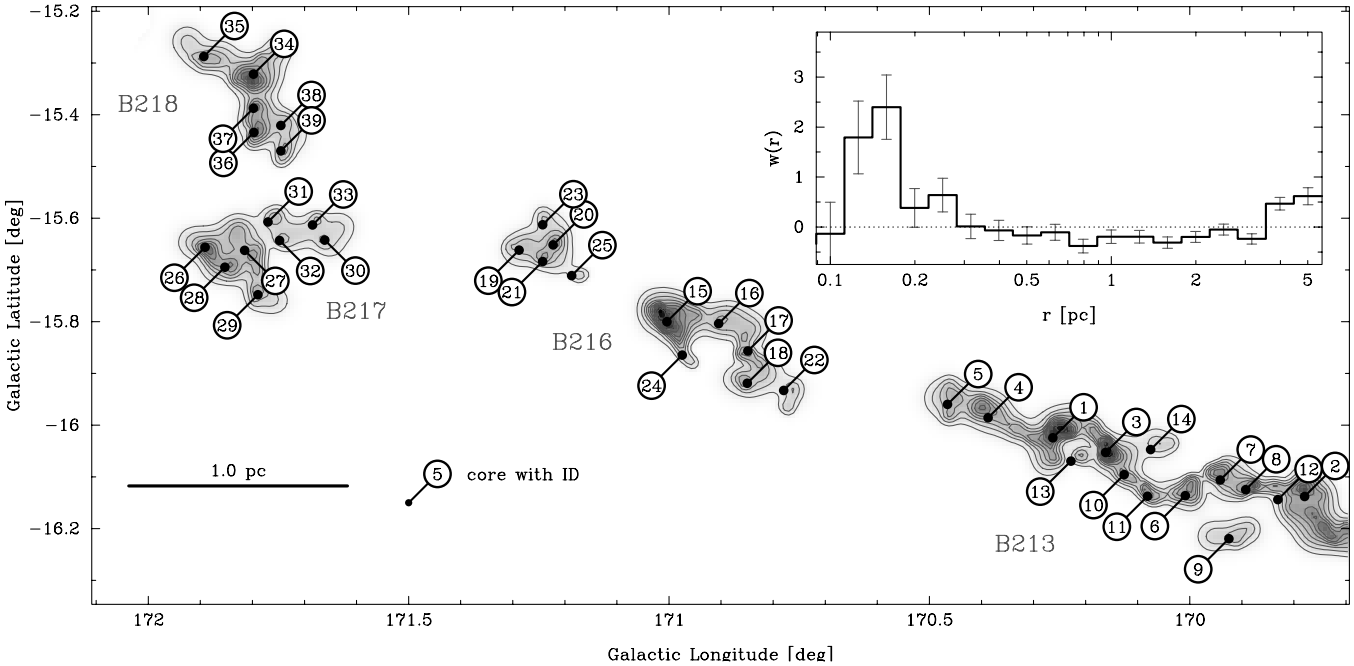

Figure 7. Distribution of cores in L 1495–E. The core-IDs can be found in Table 2. In the top right corner, the inset depicts the two-point correlation function $w(r)$.

evident (Figure 7). The latter, large separation derives from small clusters of dense cores at both ends of L 1495–E, whereas the first one represents the separation between the individual cores inside these clusters. At our pixel scale of the map, a separation of 0.15 pc corresponds to ∼7 pixels, and is, therefore, well above the resolution limit.

Core masses range from $M_{\rm core} = 0.4$ to $10\,M_\odot$. The total mass found in cores is $104 \pm 16\,M_\odot$, which makes up ∼50% of the total mass in L 1495–E (as defined by the $A_{\rm V} = 5$ mag contour). We derived mean core densities $\rho = 3\,M_{\rm core}/(4\,r_{\rm eff}^3)$, and hydrogen number densities $n_{\rm H_2} = \rho/(\mu\,m_{\rm H})$, where $m_{\rm H}$ is the proton mass and $\mu = 2.34$ is the mean molecular weight per hydrogen molecule, assuming a molecular cloud with standard composition (Lada et al. 2008). The frequency distribution of the derived number densities closely follows a Gaussian distribution with $n_{\rm H_2} = 14.3 \times 10^3$ cm^{-3} and a dispersion of 4.1×10^3 cm^{-3}.

In Figure 8, we show the mass–size relation of the cores in our sample. For reference, the figure also shows the sensitivity limit of $A_{\rm V} = 1.5$ mag for an isolated, flat, and spherical core. Lada et al. (2008) derived a slope of $M \propto r_{\rm eff}^{2.6}$ for the dense cores of the Pipe Nebula. Due to the low number of cores and the strong influence of the completeness limit on the fit, we show instead representative relations with constant column density ($M \propto r_{\rm eff}^2$), which would be predicted for clouds obeying Larson's laws (Larson 1981), and constant volume density ($M \propto r_{\rm eff}^3$), which would be expected in case of constant thermal pressure and kinetic temperature. However, with the data at hand we cannot rule out one or the other model.

The dense core mass function (DCMF), which is the number of cores per logarithmic mass interval $dN/d\log(m) \propto m^{-\Gamma}$, exhibits its maximum at $\sim 2.0\,M_\odot$, and falls off to both the low-mass and high-mass ends (Figure 9). This peak could be either true, or simply be caused due to incompleteness. However, estimating the completeness and accuracy of the DCMF is not a trivial task (see, e.g., Kainulainen et al. 2009b; Pineda et al. 2009). This is partly due to the inability of the adopted algorithm to detect cores from the variable, more-extended column density component. Partly it is also due to the noise in the map, which

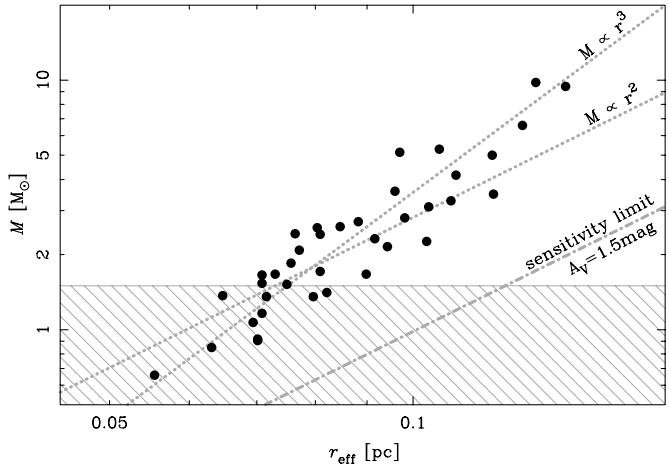

Figure 8. Mass–size relation for our cores. The hatched area marks the region of incompleteness. The dotted lines represent the cases of constant volume density $M \propto r^3$ and column density $M \propto r^2$.

makes mass determination of low-mass cores significantly less accurate than for high-mass cores. In an analysis similar to this paper, Kainulainen et al. (2009b) analyzed the accuracy derived for the cores in the Pipe Nebula, and concluded the DCMF to be accurate above about $1.2\,M_\odot$. By comparing the noise levels within these two maps we roughly estimate the DCMF to be accurate for $M_{\rm core} \geqslant 1.5\,M_\odot$. A power-law fit to the DCMF above this completeness limit yields an exponent $\Gamma = 1.2 \pm 0.2$. This slope agrees with the results of OMK02, which found $\Gamma = 1.5 \pm 0.3$ for $3 < M/M_\odot < 20$. Slopes of $\Gamma \sim 1.2$ are also commonly observed in other star-forming regions (e.g., Motte et al. 1998; Rathborne et al. 2009; André et al. 2010).

The distribution of aspect ratios R, which is defined as the ratio of the major axis versus the minor axis a/b, is strongly skewed. The mode of the distribution is found to be $R = 1.3$, whereas the mean aspect ratio is found to be $R = 1.5$, with a dispersion of 0.4 (Figure 10, left panel). Within the region of our observations, we find five cores from the sample of optically selected cores

Table 2
Dense Cores in L 1495–E

ID	l (deg)	b (deg)	$M_{\rm core}$ ($M_\odot$)	$r_{\rm eff}$ (pc)	$n_{\rm H_2}$ (10^4 cm^{-3})	Aspect Ratio R
			B 213			
1	170.26	−16.02	9.4	0.14	1.4	1.6
2	169.78	−16.14	5.3	0.11	1.8	1.2
3	170.16	−16.05	5.1	0.10	2.3	1.5
4	170.39	−15.99	5.0	0.12	1.2	1.7
5	170.47	−15.96	3.1	0.10	1.2	1.1
6	170.01	−16.14	2.7	0.09	1.6	1.2
7	169.94	−16.11	2.6	0.08	1.8	1.1
8	169.89	−16.12	2.4	0.08	1.9	1.2
9	169.93	−16.22	2.3	0.10	0.9	2.1
10	170.13	−16.10	1.8	0.08	1.8	1.3
11	170.08	−16.14	1.7	0.07	1.8	1.7
12	169.83	−16.14	1.5	0.07	1.8	2.1
13	170.23	−16.07	1.4	0.08	1.1	2.6
14	170.08	−16.05	0.9	0.07	1.1	1.2
			B 216			
15	171.00	−15.80	9.8	0.13	1.7	1.3
16	170.90	−15.80	3.3	0.11	1.0	1.7
17	170.85	−15.86	2.8	0.10	1.2	1.6
18	170.85	−15.92	2.3	0.09	1.2	1.6
19	171.29	−15.66	1.7	0.08	1.3	1.2
20	171.22	−15.65	1.7	0.07	1.9	1.2
21	171.24	−15.68	1.4	0.06	2.1	1.3
22	170.78	−15.93	0.9	0.07	1.1	1.6
23	171.24	−15.61	0.8	0.06	1.4	1.3
24	170.97	−15.86	0.7	0.06	1.6	1.4
25	171.19	−15.71	0.4	0.05	1.5	2.1
			B 217			
26	171.89	−15.66	4.2	0.11	1.3	1.2
27	171.81	−15.66	3.6	0.10	1.7	2.4
28	171.85	−15.69	2.6	0.08	2.0	1.3
29	171.79	−15.75	2.2	0.09	1.1	1.5
30	171.66	−15.64	1.7	0.09	1.0	1.8
31	171.77	−15.61	1.4	0.08	1.1	2.0
32	171.75	−15.64	1.2	0.07	1.4	1.7
33	171.68	−15.61	1.1	0.07	1.3	2.5
			B 218			
34	171.80	−15.32	6.6	0.13	1.3	1.6
35	171.89	−15.29	3.5	0.12	0.8	2.1
36	171.80	−15.43	2.4	0.08	2.2	1.1
37	171.80	−15.39	2.1	0.08	1.9	1.3
38	171.75	−15.42	1.5	0.07	1.5	1.4
39	171.75	−15.47	1.4	0.07	1.5	1.3

from Lee & Myers (1999). Three of these cores were classified as round ($R = 1$), and the remaining two had only moderate aspect ratios of $R \sim 1.8$. Compared to the all-sky sample of 406 cores from Lee & Myers (1999) with $R = 2.4 \pm 0.1$, the cores in Taurus are therefore only moderately elongated.

We also considered the orientation of the cores with respect to the filament. Due to its meandering nature, this is not a trivial task. Therefore, we first defined the baseline of the filament by setting points along its path, and then interpolated between these points using a cubic spline function. The orientation angle of the core with respect to this baseline was then obtained, and we find that the 39 cores seem to have a slight tendency to align with the filament. However, the Kolmogorov–Smirnov (KS) test results in a probability of $p = 0.46$ that this distribution is drawn from a uniform distribution. Given the large error bars on the individual orientations, which come along with the small aspect ratios, we therefore cannot draw any secure conclusions about preferential or random core alignment in this filament.

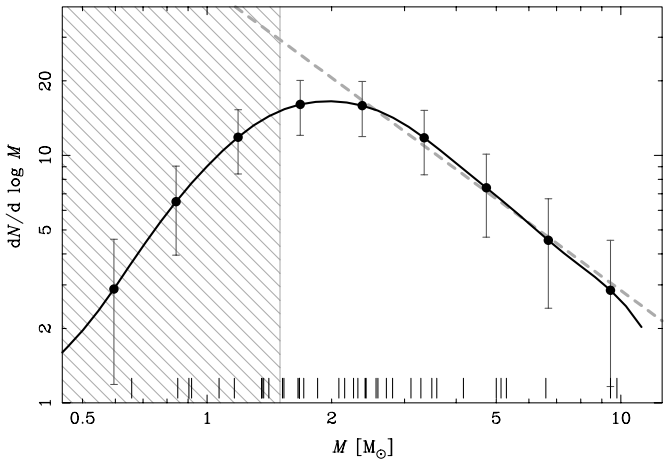

Figure 9. DCMF of L 1495–E, which was obtained by smoothing the core masses (indicated as vertical dashes along the abscissa) with a Gaussian kernel with FWHM = 0.3 dex. Points with error bars are plotted in separations of 50% of the FWHM. The dashed line shows the power-law fit with slope $\Gamma = 1.2 \pm 0.2$ for $M > 2.0\,M_\odot$. The hatched area indicates the region of incompleteness.

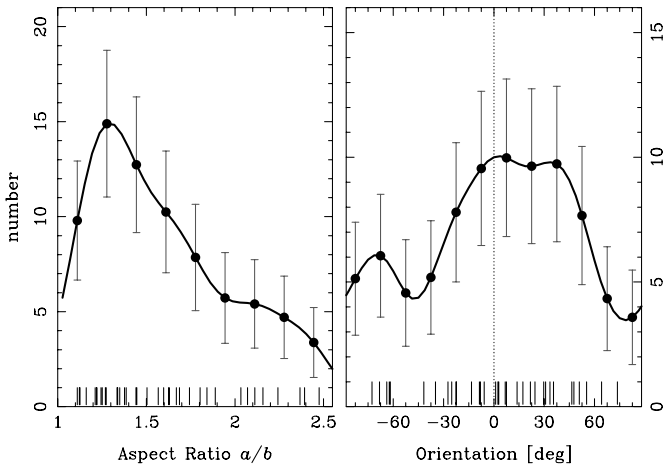

Figure 10. Left panel: distribution of aspect ratios R, which was obtained by smoothing the data points (indicated as vertical dashes on the abscissa) with a Gaussian kernel of FWHM = 0.3. Data points are plotted in steps of 50% of the FWHM. Right panel: distribution of core orientations with respect to the filament. The FWHM for the Gaussian kernel was chosen to be 30°.

3.3. Reddening Law

Algorithms like GNICER obtain the excess extinction of a source by comparing its position in the color–color diagram with respect to a control field. It is crucial for a proper estimation of extinction values to assume a reddening law (e.g., Rieke & Lebofsky 1985; Indebetouw et al. 2005). For observations in $JHK_{\rm s}$ the ratio of the color excesses

$$\alpha = \frac{E(J-H)}{E(H-K_{\rm s})} \tag{3}$$

is constant, and defines the direction of the displacement of a source in the color–color diagram when it is subjected to extinction. Therefore, the colors $(J-H)$ and $(H-K_{\rm s})$ are connected by the linear relation

$$(J-H) = \alpha(H-K_{\rm s}) + \beta. \tag{4}$$

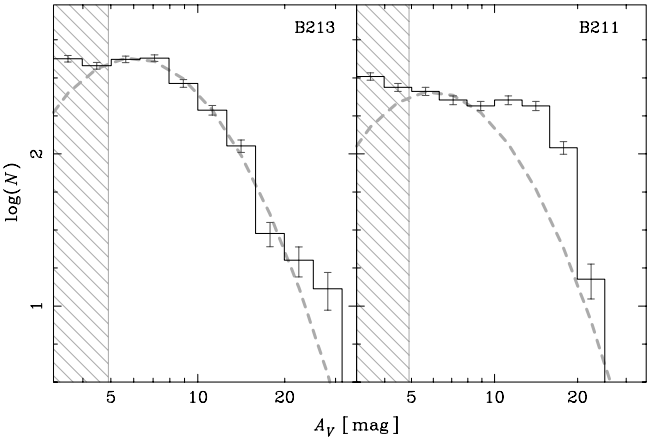

Figure 11. Column density distribution of B 213 and B 211. Our observations do not completely cover regions with $A_V < 5$ mag (hatched area). The dashed line is the lognormal fit to B 213, which is shown as a scaled-down version in the right panel.

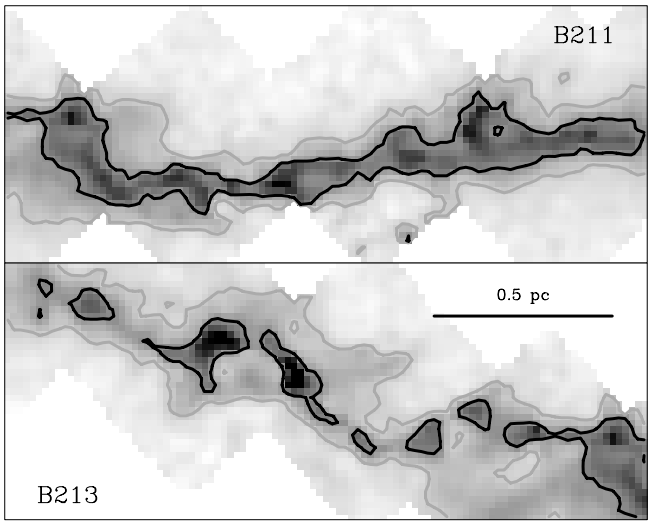

Figure 12. Zoom-ins into the regions B 211 and B 213 with contours at $A_V = 5$ mag (gray) and $A_V = 11$ mag (black).

As unreddened ZAMS stars occupy only a small region of the color–color diagram, the slope α could be simply obtained by fitting Equation (4) for all stars simultaneously. This, however, would give the high number of low-extinction stars too much weight compared to the low number of high-extinction stars. Therefore, we followed a procedure similar to Lombardi et al. (2006).

The first step was to obtain visual extinctions A_V of every star by converting color excesses $E(J - H)$ and $E(H - K_s)$ assuming the reddening law of Indebetouw et al. (2005). Stars are then binned in the color–color diagram according to their extinction A_V. These data points are then fitted according to Equation (4) to obtain a corrected slope. With the aid of this new slope, corrected extinction values A_V are then computed. This procedure is repeated until the slope α converges, which generally happened after 3–6 iterations. In order to decrease dependence on the bin size, we repeated this procedure for bin sizes ranging from $\Delta A_V = 0.5$ to 1.5 mag in steps of 0.2 mag. The best-fit slope α was then the variance weighted mean from all runs with different bin sizes.

For this analysis, we considered only sources classified as stars without any photometry flags. The best-fit slope was found to be $\alpha = 1.82 \pm 0.08$. This value is in very good agreement to the reddening laws of Lombardi et al. (2006, $\alpha = 1.82 \pm 0.03$) and Indebetouw et al. (2005, $\alpha = 1.78 \pm 0.15$).

4. DISCUSSION

4.1. Star Formation in the Filament

Due to its proximity, the Taurus Molecular Cloud is an excellent target to study the connection between filamentary structure and star formation. In this paper, we present a new, high-resolution view of the L 1495 filament, allowing characterization of its density structure down to tenth-of-a-parsec scales. Indeed, as illustrated in Figures 5–7, L 1495 shows a highly fragmented small-scale structure and in some places extinctions, which are higher than what can be traced by the chosen technique (i.e., $A_V \gtrsim 35$ mag).

To estimate the star-forming potential of the filament, we calculated the mass-per-length $M_{\rm line}$. For an undisturbed filament, filaments with a mass exceeding the critical value of $M_{\rm line}^{\rm crit} = 15\,M_\odot\,{\rm pc}^{-1}$ are prone to filamentary fragmentation and collapse (Ostriker 1964; Inutsuka & Miyama 1997). In the presence of magnetic fields, this critical value can be increased by a factor of 2 (Fiege & Pudritz 2000a). Due to the presence of dense cores, L 1495 does not really fulfill the requirement of being an undisturbed filament. However, considering only the large-scale structure, which was filtered out in the wavelet transform, we derived a value of $M_{\rm line} = 16.8 \pm 0.2\,M_\odot\,{\rm pc}^{-1}$ for the whole filament. As this must be seen as a lower limit, as some of the mass is already bound in the dense cores, this value underlines the star-forming potential of the filament.

In Figure 6, we show the previously known YSOs.[7] Interestingly, while YSOs are generally found close to dense cores in the filament, the bar-like B 211 is completely devoid of them (Goldsmith et al. 2008). Given that the mass-per-length value in this particular region is also high ($M_{\rm line} = 15\,M_\odot\,{\rm pc}^{-1}$), and that it also harbors several $H^{13}CO^+$ cores signifying the presence of high density gas ($n_{\rm crit} = 10^5\,{\rm cm}^{-3}$), it can be argued to be well underway toward star formation.

More insight into the assembly of material in the non-star-forming part of the filament can be gained by examining the distribution of column densities. Therefore, in Figure 11 we compare the quiescent B 211 with B 213, in which star formation has already occurred. The column density distribution of B 213 shows a continuous decline toward higher extinctions. In contrast, B 211 shows a flat plateau at intermediate extinctions, falling steeply at extinctions higher than $A_V \sim 13$ mag. This excess with respect to the column density distribution of B 213 can be related particularly to *inter-core* regions. This is illustrated in Figure 12, which shows the contour of $A_V = 11$ mag for both B 211 and B 213. Clearly, in B 213 such an extinction range is related to cores, while in B 211 it is more continuous and related to the material *surrounding* the cores. Therefore, we suggest that B 211 is not at all devoid of star-forming capability, but in an early stage of its evolution where the filament is fragmenting and the inter-core regions have not yet been cleared from material by accretion toward the cores. Given the high-mass reservoir in the filament, such fragmentation is inevitably leading to star formation in B 211.

In L 1495–E, the star-forming part of the filament, we investigated the spatial distribution of YSOs with respect to

[7] Rebull et al. (2010) separate YSOs into Class I, flat spectrum, Class II, and Class III. We include all YSOs, which were classified as *confirmed*, *probable*, and *possible* Taurus members in their paper.

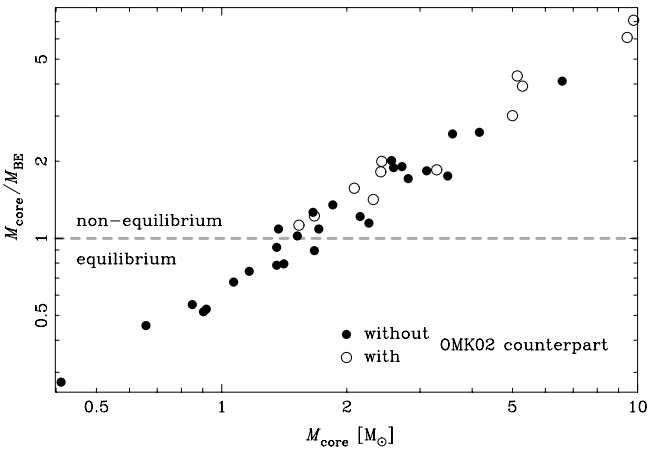

Figure 13. Ratio of core masses M_{core} to the Bonnor–Ebert critical mass M_{BE} plotted against core mass. M_{BE} was calculated individually for every core, assuming its respective density and a temperature of $T = 10$ K. Open circles represent cores which have a counterpart from the dense core sample of OMK02.

the filament. Class I and flat-spectrum sources are found at extinctions of $A_V = 8.2 \pm 3.0$ mag, which is higher compared to the extinctions at the positions of Classes II and III ($A_V = 5.2 \pm 2.6$ mag). The mean spatial separation of Class I and flat-spectrum sources from the filament was found to be only 0.06 pc, whereas older sources showed considerably larger mean distances. To verify whether this could be a pure evolutionary effect, we performed a simple Monte Carlo simulation to model the time dependence of the spatial distribution of sources. We distributed 10,000 test sources with a three-dimensional velocity dispersion of 0.2 km s^{-1} $\sim$ 0.2 pc Myr^{-1} along the baseline of the filament (defined in Section 3.2). The mean distance of sources from the filament was then measured as a function of time. The test sources started to show larger mean distances than Class I and flat-spectrum sources after $\sim$1 Myr. A mean distance similar to that of Class II and Class III objects was reached after $\sim$3.5 Myr, which is in good agreement with the evolutionary timescale of these sources (Luhman et al. 2003, 2009).

4.2. The Nature of the Dense Cores

In Section 3.2, we defined and examined the dense core population in L 1495–E. To test whether these cores are gravitationally bound entities, one can estimate the Bonnor–Ebert critical mass (Lada et al. 2008)

$$M_{BE} \sim 1.82 \left(\frac{n_{H_2}}{10^4\ \mathrm{cm}^{-3}}\right)^{-1/2} \left(\frac{T}{10\,\mathrm{K}}\right)^{3/2} M_\odot.$$

Within this framework, in cores with $M_{core} > M_{BE}$ thermal motions do not provide enough support against gravity, and in the absence of other forces they inevitably collapse and form protostars. With a mean density of $n_{H_2} = 1.5 \times 10^4$ cm^{-3} and a temperature of $T = 10$ K (Terebey et al. 2010), we obtain $M_{BE} = 1.5\,M_\odot$. Calculating the Bonnor–Ebert critical mass for all cores allowed us to analyze the stability of each core separately (Figure 13). As a result we find that in L 1495–E, the majority of cores is prone to collapse. Without exception, all cores that coincide with a dense $H^{13}CO^+$ core (OMK02) exhibit $M_{core} > M_{BE}$. Apparently, in these cores the collapse has already led to a density enhancement, which can be traced by $H^{13}CO^+$ with its critical density of $n_{crit} \sim 10^5$ cm^{-3}.

Compared, e.g., to the starless core population in the Pipe Nebula ($n_{H_2} = 7.3 \times 10^3$ cm^{-3}; Lada et al. 2008), the cores in the Taurus filament are clearly denser by a factor of 2. For the cores in the Pipe Nebula, the Bonnor–Ebert critical mass is $\sim$2 $M_\odot$ (assuming $T = 10$ K), and only a few cores exceed this value and are prone to collapse. Cores in Taurus are also considerably more clustered than those in the Pipe Nebula. The nearest neighbor separation and two-point correlation function (Figure 7) show a clear peak at separations of the order of 0.13 pc, whereas cores in the Pipe Nebula show separations of 0.38 pc (Rathborne et al. 2009). Fragmentation in Taurus happens mainly only on a very distinct spatial scale. In the case of thermal fragmentation, such a preferential length scale would be determined by the Jeans length

$$\lambda_J = c_s \left(\frac{\pi}{G\rho}\right)^{1/2}, \quad (5)$$

where c_s is the local sound speed, G is the gravitational constant, and ρ is the mass density. Assuming $c_s = 0.19$ km s^{-1} ($T = 10$ K) and the mean mass density of our sample of cores ($\rho = 5.8 \times 10^{-26}$ g cm^{-3}) we derive $\lambda_J = 0.18$ pc, which is only slightly larger than the peak in the nearest neighbor distribution of 0.13 pc. This is in contrast to the Pipe Nebula with a separation of 0.38 pc (Rathborne et al. 2009), which exceeds its local Jeans length ($\lambda_J \sim 0.25$ pc).

We note that due to the unknown inclination angle i we can only derive the *projected* nearest neighbor separation, but the true separation between cores remains unclear. For $i \sim 45°$ the true nearest neighbor separation would match the local Jeans length. Very Long Baseline Array observations allow accurate distance measurements of selected stars in the Taurus Molecular Cloud exist (Loinard et al. 2007; Torres et al. 2007, 2009), but do not allow us to estimate the true spatial orientation of the filament.

We note, that non-zero inclination angles would not only affect the derived nearest neighbor separation, but also the aspect ratio. Randomly oriented cores would yield the observed mean aspect ratio of $R = 1.5$, if the true aspect ratio is $R_{true} \sim 1.7$ in the case of prolate, and $R_{true} \sim 2.2$ for oblate cores, respectively (Myers et al. 1991). However, from a large set of dense cores and Bok globules, Ryden (1996) argues that cores are generally rather prolate than oblate. This shape is furthermore supported by theoretical simulations (Fiege & Pudritz 2000b), where helical magnetic fields are able to produce a population of prolate dense cores through filamentary fragmentation. The aspect ratios of these cores are in good agreement with the sample of Ryden (1996), who finds $R = 2.0$–2.5. Therefore, under the assumption of prolate cores, we find cores which are slightly more spherical ($R_{true} \sim 1.7$). The same trend is visible, when comparing the Taurus cores from the sample of Lee & Myers (1999) to their galactic average. Whether this is truly the case, or simply a projectional effect cannot be determined. Due to the core formation in the filament, we do not expect our sample of cores to be oriented randomly, but rather inheriting some preferential direction. However, the meandering nature of the filament does not allow us to determine a common inclination angle. Considering these limitations, the elongation of our cores agrees reasonably well with theoretical predictions and other observations.

5. SUMMARY

In this paper, we study the star formation in the Taurus filament L 1495. In particular, we present an NIR extinction map of this filament with unprecedented dynamical range

($A_V \sim 1.5$–35 mag) and resolution (0.″9). The main results of this paper are as follows.

1. The extinction map of L 1495 reveals the highly fragmented nature of the filament, harboring a population of dense cores preferentially separated by the local Jeans length. The mass-per-length in the filament is $M_{\rm line} = 17\,M_\odot\,{\rm pc}^{-1}$, indicative of its star-forming potential. We find that the part of the filament that harbors no YSOs, namely B 211, shows an internal structure different from that of the rest of the filament. We argue that B 211 is still younger than other parts of the filament, being still in process of filament fragmentation. Given its high mass reservoir, star formation will inevitably ensue.
2. The dense core population in L 1495–E was investigated in detail. A total of 39 dense cores with masses between $M_{\rm core} = 0.4$ and $10\,M_\odot$ and densities of $n_{\rm H_2} = 1.5 \times 10^4\,{\rm cm}^{-3}$ were found. The majority of these cores exceeds the critical mass for collapse $M_{\rm BE}$, and is therefore prone to collapse. The high-mass tail of the DCMF can be fitted with a power law with an exponent $\Gamma = 1.2 \pm 0.2$, a form commonly observed also in other star-forming regions.

We thank Calar Alto Observatory for allocation of director's discretionary time to this program, and the anonymous referee for her/his constructive suggestions that helped to improve the manuscript. This material is based upon work supported by the National Science Foundation under Grant No. AST-0908159. This publication makes use of data products from the Two Micron All Sky Survey (Skrutskie et al. 2006), which is a joint project of the University of Massachusetts and the Infrared Processing and Analysis Center/California Institute of Technology, funded by the National Aeronautics and Space Administration and the National Science Foundation. We furthermore acknowledge the use of NASA's SkyView facility (http://skyview.gsfc.nasa.gov) located at NASA Goddard Space Flight Center (McGlynn et al. 1998) and the ViZier database located at CDS in Strasbourg, France (Ochsenbein et al. 2000).

Facility: CAO:3.5m (Omega2000)

REFERENCES

Alves, J., Lombardi, M., & Lada, C. J. 2007, A&A, 462, L17
André, P., et al. 2010, A&A, 518, L102
Barnard, E. E. 1927, Catalogue of 349 Dark Objects in the Sky (Chicago: Univ. Chicago Press)
Barnard, E. E., Frost, E. B., & Calvert, M. R. 1927, A Photographic Atlas of Selected Regions of the Milky Way (Washington: Carnegie Institution of Washington)
Bergin, E. A., & Tafalla, M. 2007, ARA&A, 45, 339
Bertin, E., & Arnouts, S. 1996, A&AS, 117, 393
Bohlin, R. C., Savage, B. D., & Drake, J. F. 1978, ApJ, 224, 132
Cantiello, M., Blakeslee, J. P., Raimondo, G., Mei, S., Brocato, E., & Capaccioli, M. 2005, ApJ, 634, 239
Dobashi, K., Uehara, H., Kandori, R., Sakurai, T., Kaiden, M., Umemoto, T., & Sato, F. 2005, PASJ, 57, 1
Fassbender, R. 2003, Diploma thesis, Univ. Heidelberg
Fiege, J. D., & Pudritz, R. E. 2000a, MNRAS, 311, 85
Fiege, J. D., & Pudritz, R. E. 2000b, ApJ, 534, 291
Foster, J. B., Román-Zúñiga, C. G., Goodman, A. A., Lada, E. A., & Alves, J. 2008, ApJ, 674, 831
Goldsmith, P. F., Heyer, M., Narayanan, G., Snell, R., Li, D., & Brunt, C. 2008, ApJ, 680, 428
Gooch, R. 1996, in ASP Conf. Ser. 101, Astronomical Data Analysis Software and Systems V, ed. G. H. Jacoby & J. Barnes (San Francisco, CA: ASP),
Goodman, A. A., Pineda, J. E., & Schnee, S. L. 2009, ApJ, 692, 91
Hartmann, L. 2002, ApJ, 578, 914
Henning, T., Linz, H., Krause, O., Ragan, S., Beuther, H., Launhardt, R., Nielbock, M., & Vasyunina, T. 2010, A&A, 518, L95
Indebetouw, R., et al. 2005, ApJ, 619, 931
Inutsuka, S.-I., & Miyama, S. M. 1997, ApJ, 480, 681
Jijina, J., Myers, P. C., & Adams, F. C. 1999, ApJS, 125, 161
Johnstone, D., Wilson, C. D., Moriarty-Schieven, G., Joncas, G., Smith, G., Gregersen, E., & Fich, M. 2000, ApJ, 545, 327
Kainulainen, J., Beuther, H., Henning, T., & Plume, R. 2009a, A&A, 508, L35
Kainulainen, J., Lada, C. J., Rathborne, J. M., & Alves, J. F. 2009b, A&A, 497, 399
Kainulainen, J., Lehtinen, K., & Harju, J. 2006, A&A, 447, 597
Kainulainen, J., Lehtinen, K., Väisänen, P., Bronfman, L., & Knude, J. 2007, A&A, 463, 1029
Kenyon, S. J., Gómez, M., & Whitney, B. A. 2008, in Handbook of Star Forming Regions, Vol. I, ed. B. Reipurth (San Francisco, CA: ASP), 405
Lada, C. J., Lada, E. A., Clemens, D. P., & Bally, J. 1994, ApJ, 429, 694
Lada, C. J., Muench, A. A., Rathborne, J., Alves, J. F., & Lombardi, M. 2008, ApJ, 672, 410
Larson, R. B. 1981, MNRAS, 194, 809
Lee, C. W., & Myers, P. C. 1999, ApJS, 123, 233
Loinard, L., Torres, R. M., Mioduszewski, A. J., Rodríguez, L. F., González-Lópezlira, R. A., Lachaume, R., Vázquez, V., & González, E. 2007, ApJ, 671, 546
Lombardi, M. 2009, A&A, 493, 735
Lombardi, M., & Alves, J. 2001, A&A, 377, 1023
Lombardi, M., Alves, J., & Lada, C. J. 2006, A&A, 454, 781
Lombardi, M., Lada, C. J., & Alves, J. 2010, A&A, 512, A67
Luhman, K. L., Briceño, C., Stauffer, J. R., Hartmann, L., Barrado y Navascués, D., & Caldwell, N. 2003, ApJ, 590, 348
Luhman, K. L., Mamajek, E. E., Allen, P. R., & Cruz, K. L. 2009, ApJ, 703, 399
Lynds, B. T. 1962, ApJS, 7, 1
McGlynn, T., Scollick, K., & White, N. 1998, in IAU Symp. 179, New Horizons from Multi-Wavelength Sky Surveys, ed. B. J. McLean, et al. (Cambridge: Cambridge Univ. Press), 465
Men'shchikov, A., et al. 2010, A&A, 518, L103
Mizuno, A., Onishi, T., Yonekura, Y., Nagahama, T., Ogawa, H., & Fukui, Y. 1995, ApJ, 445, L161
Molinari, S., et al. 2010, A&A, 518, L100
Motte, F., Andre, P., & Neri, R. 1998, A&A, 336, 150
Myers, P. C. 2009, ApJ, 700, 1609
Myers, P. C., Fuller, G. A., Goodman, A. A., & Benson, P. J. 1991, ApJ, 376, 561
Narayanan, G., Heyer, M. H., Brunt, C., Goldsmith, P. F., Snell, R., & Li, D. 2008, ApJS, 177, 341
Ochsenbein, F., Bauer, P., & Marcout, J. 2000, A&AS, 143, 23
Onishi, T., Mizuno, A., Kawamura, A., Ogawa, H., & Fukui, Y. 1998, ApJ, 502, 296
Onishi, T., Mizuno, A., Kawamura, A., Tachihara, K., & Fukui, Y. 2002, ApJ, 575, 950
Ostriker, J. 1964, ApJ, 140, 1056
Palla, F., & Stahler, S. W. 2002, ApJ, 581, 1194
Pilbratt, G. L., et al. 2010, A&A, 518, L1
Pineda, J. E., Caselli, P., & Goodman, A. A. 2008, ApJ, 679, 481
Pineda, J. E., Rosolowsky, E. W., & Goodman, A. A. 2009, ApJ, 699, L134
Quanz, S. P., Goldman, B., Henning, T., Brandner, W., Burrows, A., & Hofstetter, L. W. 2010, ApJ, 708, 770
Rathborne, J. M., Lada, C. J., Muench, A. A., Alves, J. F., Kainulainen, J., & Lombardi, M. 2009, ApJ, 699, 742
Rebull, L. M., et al. 2010, ApJS, 186, 259
Rieke, G. H., & Lebofsky, M. J. 1985, ApJ, 288, 618
Román-Zúñiga, C. G., Lada, C. J., & Alves, J. F. 2009, ApJ, 704, 183
Rosolowsky, E. W., Pineda, J. E., Kauffmann, J., & Goodman, A. A. 2008, ApJ, 679, 1338
Ryden, B. S. 1996, ApJ, 471, 822
Sadavoy, S. I., et al. 2010, ApJ, 710, 1247
Schneider, S., & Elmegreen, B. G. 1979, ApJS, 41, 87
Siess, L., Dufour, E., & Forestini, M. 2000, A&A, 358, 593
Skrutskie, M. F., et al. 2006, AJ, 131, 1163
Stutzki, J., & Guesten, R. 1990, ApJ, 356, 513
Terebey, S., Fich, M., Noriega-Crespo, A., Padgett, D., & Taurus Spitzer Legacy Team 2010, BAAS, 41, 559
Torres, R. M., Loinard, L., Mioduszewski, A. J., & Rodríguez, L. F. 2007, ApJ, 671, 1813
Torres, R. M., Loinard, L., Mioduszewski, A. J., & Rodríguez, L. F. 2009, ApJ, 698, 242
Vasyunina, T., Linz, H., Henning, T., Stecklum, B., Klose, S., & Nyman, L.-Å. 2009, A&A, 499, 149
Williams, J. P., de Geus, E. J., & Blitz, L. 1994, ApJ, 428, 693